GPPS | JOURNAL

JOURNAL OF THE GLOBAL POWER AND PROPULSION SOCIETY
journal.gpps.global

Decarbonisation of high-temperature endothermic chemical reaction processes using a novel turbomachine: robustness of the concept to feed variability

Original article

Article history:
Submission date: 14 November 2023
Acceptance date: 4 March 2024
Publication date: 30 April 2024

This is the updated version of a paper originally presented at the Global Power and Propulsion Technical Conference, GPPS Hong Kong23, October 17–19, 2023.

Check for updates

***Correspondence:**
DR: dylan.rubini@eng.ox.ac.uk

Peer review:
Single blind

Copyright:
© 2024 Rubini et al. This is an open access article distributed under the Creative Commons Attribution Non Commercial No Derivatives License (CC BY-NC-ND 4.0). Unrestricted use, distribution, and reproduction of the original work are permitted for noncommercial purposes only, provided it is properly cited and its authors credited. No derivative of this work may be distributed.

Keywords:
compressor aerodynamics; chemical reactions; computational fluid dynamics; turbo-reactor; rotordynamic reactor; turbomachinery design

Citation:
Rubini D., Karefyllidis N., Rosic B., Xu L., and Nauha E. (2024). Decarbonisation of high-temperature endothermic chemical reaction processes using a novel turbomachine: robustness of the concept to feed variability. Journal of the Global Power and Propulsion Society. 8: 111–126. https://doi.org/10.33737/jgpps/185623

OPEN ACCESS

Dylan Rubini[1,*], Nikolas Karefyllidis[1], Budimir Rosic[1], Liping Xu[2], Elina Nauha[3]

[1]*Oxford Thermofluids Institute, University of Oxford, Oxford OX1 3PJ, UK*
[2]*Whittle Laboratory, University of Cambridge, Cambridge CB3 0DY, UK*
[3]*Coolbrook Oy, Pieni Roobertinkatu 9 00130, Helsinki, Finland*

Abstract

This paper presents a revolutionary turbomachinery concept, referred to as the turbo-reactor, which has the potential to replace gas-fired radiant furnaces and decarbonise a wide range of hard-to-abate, high-temperature endothermic chemical reaction processes. Although previous studies by the authors have confirmed the feasibility of using a turbo-reactor for steam cracking reactions, the numerical investigation presented in this work broadens the scope of potential applications for the machine to a variety of energy-intensive chemical processes, including those used for hydrogen production. This step change in technology could be the catalyst needed to enable rapid scale-up of low-carbon hydrogen technology. The innovative design of the turbo-reactor is fundamentally based on converting all of the imparted mechanical energy into internal energy, rather than pressure. This enables temperatures of up to 1,700°C to be achieved within an axial length on the order of one metre, resulting in an increase in the power density of 50 to 1,000 times compared to a surface heat exchanger. This paper presents the first comprehensive analysis of the turbo-reactor's robustness and controllability across a broad spectrum of feeds, chemical reaction stages, Mach number regimes, and operating points, conclusively demonstrating the feasibility of a universal stage design strategy for repeatedly imparting and dissipating energy for various endothermic reaction processes.

Introduction

Motivation and background

Decarbonisation of hard-to-abate high-temperature endothermic chemical reaction processes, such as steam cracking of hydrocarbons, ethylene dichloride cracking, plastic recycling, hydrogen production through steam methane reformation (SMR), and ammonia decomposition, is a significant challenge of this decade (Thiel and Stark, 2021). These processes are essential components of large-scale global industries. For example, the hydrocarbon cracking market was recently valued at $240 billion, with a global annual capacity of 400 million tons per annum (Mtpa) (Bender, 2014). This is expected to grow to $350 billion, with a capacity of 600 Mtpa, by 2030. Furthermore, with the rapidly growing support for low-carbon hydrogen and ammonia for transport, industry, energy storage, and power generation, it is expected that their demand will increase exponentially, potentially reaching to 200 Mtpa by 2030, with a market value of $320 billion (IEA, 2022).

The primary challenge is that large-scale energy-intensive sectors (e.g., chemical/petrochemicals steel, and cement) account for almost 20% of global CO_2 emissions (IEA, 2021), mainly due to heat generated by fossil fuel combustion. To address this challenge, a new class of turbomachines has been developed to replace gas-fired surface heat exchangers (specifically the firebox/furnace unit) used in these industrial processes, as shown in Figure 1.

Heavy industry can be transformed radically by exploiting the complex flow physics and controllable energy conversion processes possible within a turbomachine. This novel turbomachine, known as the RotoDynamic Reactor (RDR) or turbo-reactor, works on the principle of directly imparting mechanical energy to the working fluid supplied by a renewably powered electric motor as the mechanical driver (Rubini et al., 2021; Coolbrook Oy, 2022). As a result, Figure 1 demonstrates that the turbo-reactor can significantly increase power density by up to two orders of magnitude compared to a surface heat exchanger, leading to a reduced plant footprint, as well as lower capital, operating, and maintenance costs. This is achieved by converting almost all of the imparted mechanical energy into internal energy, rather than compressing the gas as is done in a compressor (which is another example of an energy-imparting machine). Therefore, high working fluid temperatures of up to 1700°C can be achieved within short axial distances of less than one metre, depending on the working fluid properties. This can result in a significant improvement in the efficiency and yield of the reaction (Rubini et al., 2022b). Previous work by the authors presents a detailed introduction and analysis of stage design, energy transformation train, and fundamental flow physics (Rubini et al., 2021, 2022a,b; Karefyllidis et al., 2023).

Figures 2 and 3 highlight the significant role of the RDR in decarbonising a diverse set of high-temperature endothermic reaction processes for the production of high-value commodity chemicals in the chemical industry, such as steam cracking, thermochemical plastic waste recycling, SMR for hydrogen production, and ammonia decomposition for hydrogen recovery. Alternative strategies to decarbonise these sectors include hydrogen-fired (Weydahl et al., 2013) or electric furnaces (Delikonstantis et al., 2019), but these suffer from large thermal resistances that hinder energy transfer (Venkataraman et al., 2003), low power density, and non-uniform temperature profiles within the tubes, all of which can degrade the efficiency of the process. Furthermore, there are additional

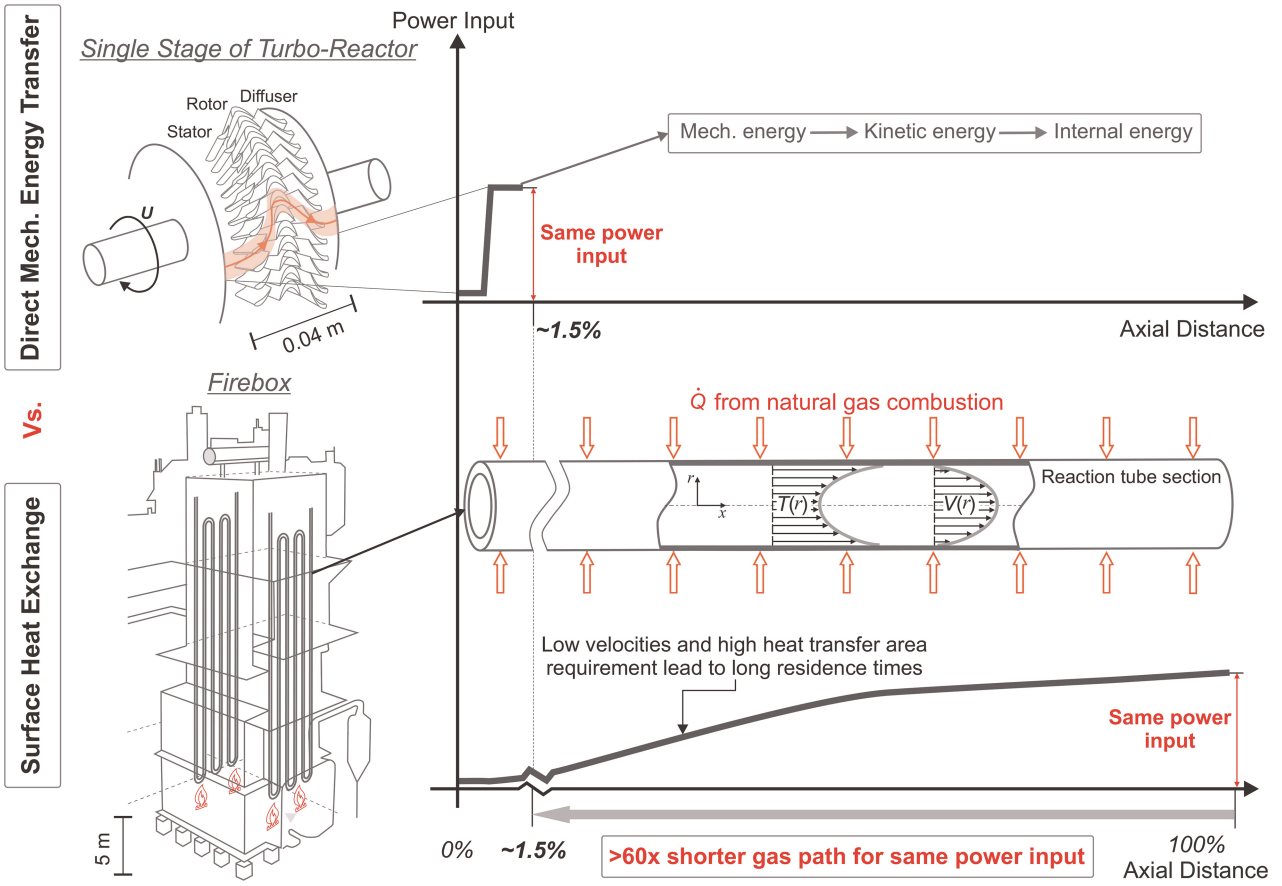

Figure 1. A schematic analysis of the energy transfer mechanism in a surface heat exchanger against that in the turbo-reactor.

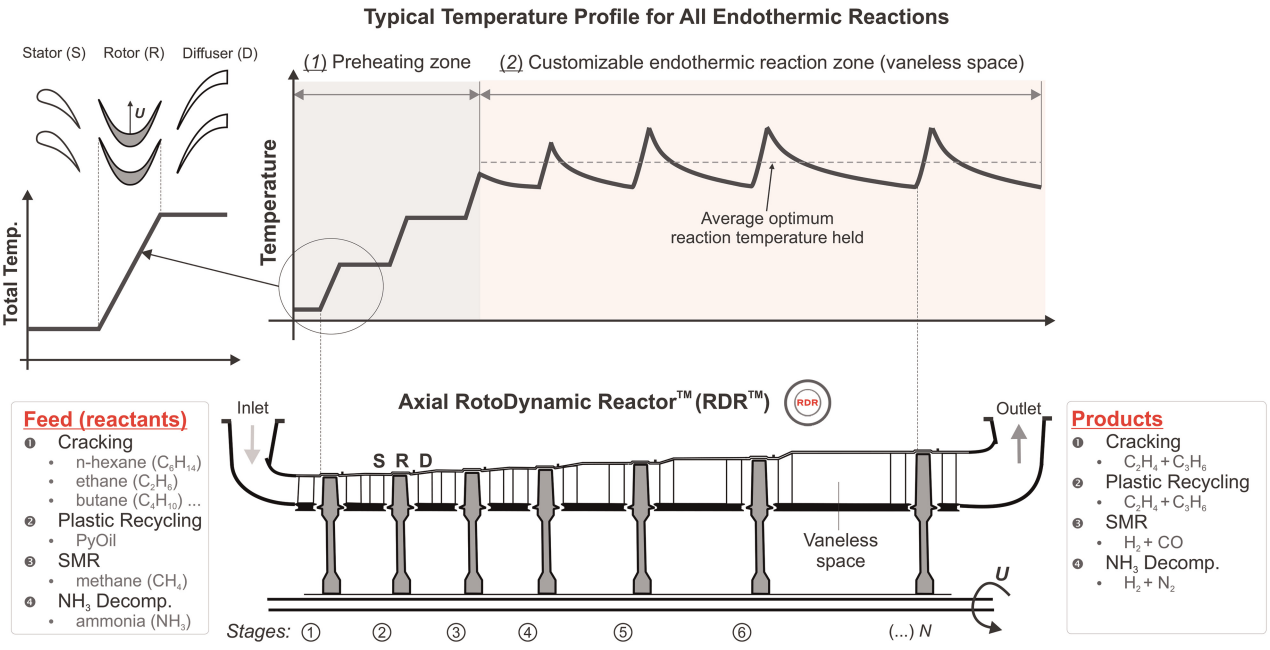

Figure 2. A schematic of the elemental stage and multistage environment for the RotoDynamic Reactor, illustrating a typical temperature profile for some example endothermic chemical processes that could be driven by the RDR.

challenges related to scalability at high temperatures for electric furnaces and low energy conversion efficiency $\leq 60\%$ (Lu et al., 2022) and nitrous oxide emissions for hydrogen-fired furnaces.

Objectives of this study

This first-of-its-kind paper demonstrates the applicability of the RDR for decarbonising a wide range of endothermic reactions within the chemical industry (see Figure 3). This study confirms the robustness and controllability of the system subjected to different feedstocks, variable reaction states, and a range of operating points. A broad spectrum of operating states is generated by harnessing variations in thermophysical/thermochemical fluid properties corresponding to different feedstocks (e.g., n-hexane, methane, etc.) and reaction progress states. The RDR is shown to be resilient and flexible, and energy can be effectively imparted and dissipated despite using a fixed stage design and boundary conditions.

The turbo-reactor: direct energy transfer for endothermic chemical reactions

Controllable elemental stage design for ultra-high power density energy input

The turbo-reactor concept and detailed design have been developed over many years of collaboration with Coolbrook Oy (2022) and are based on the original patent of Bushuev (2016). This new machine unlocks a radically new design space for high-power-density energy-imparting machines, as shown in Figures 2 and 4. Figure 4 compares the single-stage constant speed $\phi - \psi$ and $\phi - C_{\psi_{TS}}$ characteristics between the turbo-reactor and an axial compressor. As the primary objective of an axial compressor is the increase of pressure, the work coefficient ψ is limited by isentropic efficiency constraints throughout the operating range (see Figure 4b), and system instability considerations at low flow coefficients ϕ (see Figure 4c). For the RDR, by eliminating the requirement for an increase in static pressure, these constraints are bypassed within the relevant operating range (that is, $p_{exit}/p_{0,in} \leq 1$). This results in the following key design differences from a compressor:

1. For low molecular weight fluids, an ultra-high loading coefficient of up to 8.0 is possible (see Figure 4b). This is more an order of magnitude higher than that of a typical axial compressor, minimising the number of stages required for heating. Figure 4b indicates that the work coefficient increases approximately linearly with the flow coefficient, before turning to the vertical due to feed-composition-dependent choking limitations.
2. Within the choking limits of the working fluid, the RDR can leverage very high relative Mach numbers $\phi \approx 1.0$ and flow coefficients (up to $\phi \approx 1.0$) without the risk of system instability and overall performance

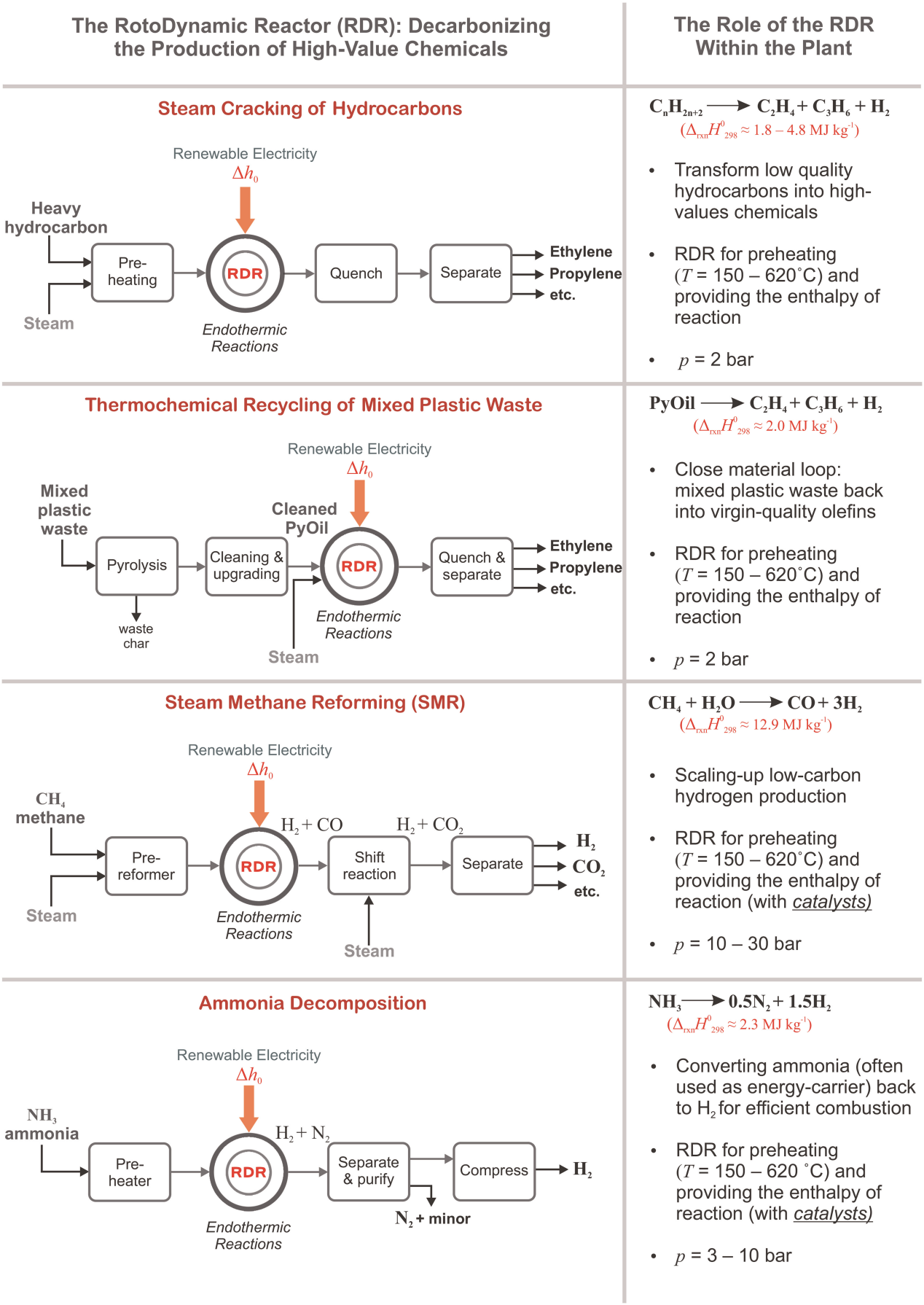

Figure 3. Schematic illustration of potential opportunities for turbomachines to decarbonise high-temperature endothermic reaction processes in the chemical and petrochemical industry.

degradation. This enables a high flow capacity per unit frontal area, resulting in a smaller machine footprint.

3. Since there is no requirement to support a global adverse pressure gradient, Figure 4c illustrates that the onset condition for violent dynamic system instability is circumvented as $(\partial C_{\psi_{TS}}/\partial\phi) < 0$ (Greitzer et al., 2007). Therefore, the RDR is robust, controllable, and inherently free of large-scale system instability (i.e., negative aerodynamic damping) over a wide range of operating states. However, it is noted that local instability may still grow within certain blade rows.

These features are achieved by imparting almost all the available exergy into the fluid as kinetic energy (KE) using high-turning supersonic impulse rotor blades (see Figure 2) rather than pressurising the gas. Through aerodynamic losses, this KE is then rapidly dissipated into internal energy within the diffuser and vaneless space. This allows very high temperatures to be attained in a fraction of a millisecond without a pressure rise across the stage. For example, a temperature change greater than 300 °C per stage can be achieved with air as the working fluid. As a result, the flow path length required to heat a given mass of fluid to a specified temperature can be reduced by nearly two orders of magnitude compared to a furnace (see Figure 1).

In a multistage environment, the flow must be reconditioned before the next rotor row. A stator vane is used to rapidly accelerate the flow to help it recover before entering the downstream row and to provide the necessary high Mach number with a large negative swirl angle (to the rotor). The favourable pressure gradient attenuates residual flow non-uniformities from the upstream mixing process, ensuring high performance across the multistage architecture (Karefyllidis et al., 2023).

Addressing the limitations of surface heat exchange

Compared to radiant furnaces, the RDR provides a fundamental advantage: mechanical energy is directly transferred into the fluid, making it the hottest part of the system. This is in contrast to furnaces, where the walls are the hottest part of the system due to the heat transfer process. This inherent feature of volumetric energy addition bypasses two key challenges encountered in radiant coils. First, the heat transfer area requirement is avoided, allowing a significantly shorter gas path (see Figure 1). Reaction selectivity is a function of residence time; therefore, the primary product yield can be increased.

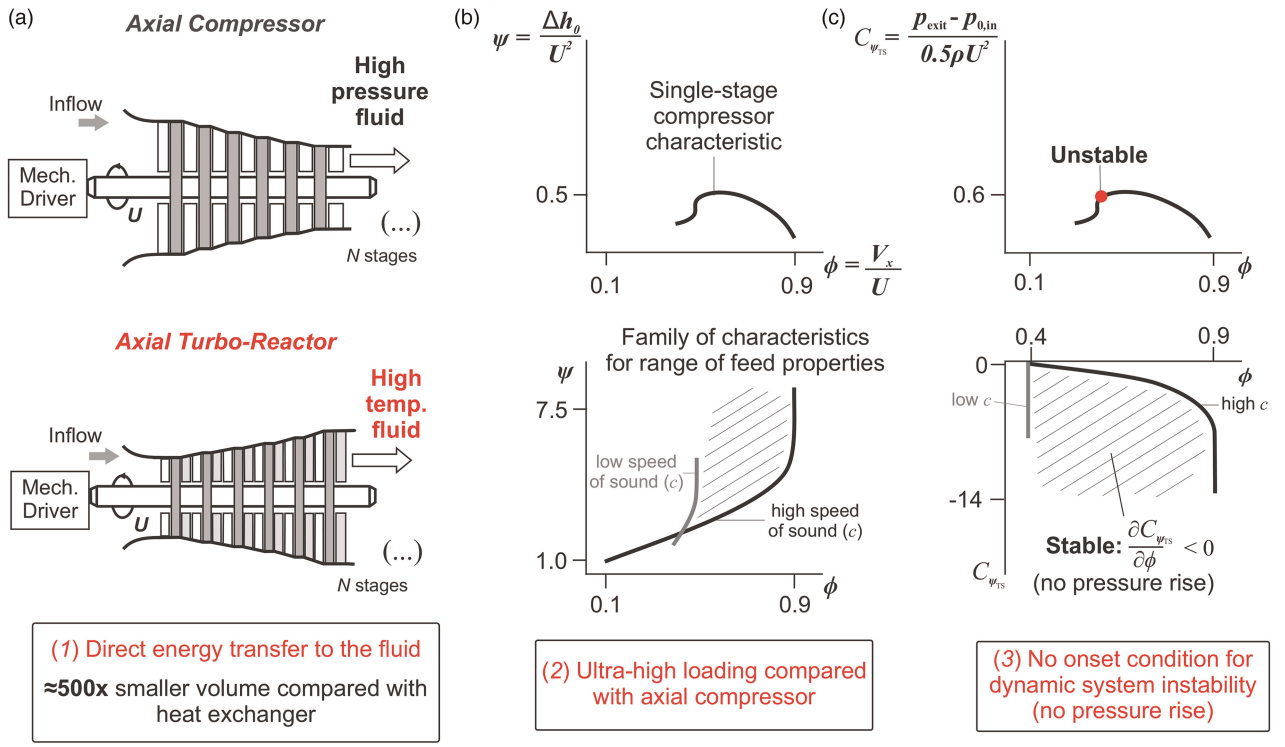

Figure 4. A comparison between an axial compressor and turbo-reactor (both energy imparting machines), showing (a) the primary objectives, (b) the single-stage flow coefficient ϕ against stage loading ψ characteristic speedline, and (c) the single-stage flow coefficient ϕ against total-to-static pressure rise coefficient $C_{\psi_{TS}}$ characteristic.

Second, as indicated in Figure 1, the thermal and velocity boundary layers within the tubes are thick and mismatched. As a result, the majority of the fluid's mass is concentrated at the centre, but the highest temperature is at the surface. This results in coke deposition on the walls due to high metal temperatures (for hydrocarbon feeds) and overcracking due to nonhomogeneous reaction progress. By avoiding these limitations, the RDR enables a more homogeneous and efficient reaction for all chemical processes, as well as lower coking rates for hydrocarbon-based feeds.

Fine-tuned control of the endothermic reaction dynamics

For high-temperature endothermic chemical reactions, where the enthalpy of reaction $\Delta_{\mathrm{rxn}}H^0_{298}$ is positive, a turbomachine can be used to replace conventional radiant furnaces. The turbo-reactor preheats the gas mixture to a temperature where the reaction proceeds efficiently, followed by further customised stages to maintain the average optimum reaction temperature during the subsequent enthalpy-draining reaction, as shown in Figure 2. This paper will show the versatility of the RDR using four example applications (see Figure 3) summarised below.

1. Steam cracking: transforming heavy hydrocarbons into higher-value olefins such as ethylene (C_2H_4) and propylene (C_2H_6). This is a thermal decomposition (i.e., pyrolysis) reaction in an oxygen-free environment.
2. Thermochemical recycling of mixed plastic waste (Kusenberg et al., 2022): decomposing pyrolysis oil (PyOil) back into virgin-quality olefins (see Figure 3). PyOil is converted to olefins using the same process mentioned above (see 1.).
3. Steam methane reforming: the RDR is used to produce syngas ($CO + H_2$) from natural gas (CH_4). This syngas is processed and separated into hydrogen (H_2) and carbon dioxide (CO_2) (Rostrup-Nielsen and Christiansen, 2011).
4. Ammonia (NH_3) decomposition: converting ammonia into hydrogen (H_2), which is becoming an important process to release H_2 from an ammonia energy carrier for cleaner and more efficient combustion (Jackson et al., 2019).

A common feature among the working fluids used in these applications is that they are all superheated vapours following the ideal gas law with a temperature-dependent isobaric heat capacity (i.e., the mixture is a semi-perfect gas). In the first three applications, superheated steam is added to the feed to reduce the coke (i.e., solid carbon) deposition on the surfaces. Therefore, steam plays a crucial role in determining the properties of the mixture. The fact that the mixture is a single-phase, semi-perfect gas (rather than a non-ideal fluid) significantly simplifies turbomachinery design and modelling processes.

The objective of the non-reacting, ultra-fast preheating section ($150\ ^\circ\mathrm{C} \leq T \leq 620\ ^\circ\mathrm{C}$) for all chemical processes is to maximise the flow of energy into the fluid within a minimum distance and time scale. In some configurations of the preheating zone, the vaneless space can be eliminated by integrating the diffuser and the stator. As a result, the flow can enter successive stages with a higher and higher flow coefficient, enabling a potential increase in stage loading across the multistage architecture (until an equilibrium is reached).

Once preheating is complete and the gas mixture is at the reaction activation temperature, the vapour enters the reaction zone where the turbo-reactor provides a tailored temperature profile based on the application-specific reaction dynamics (see Figure 2). This is achieved using a non-uniform axial distribution for the interstage vaneless space length (see Figure 2). For each stage, the axial dimension depends on the local heat of reaction, which is a function of the thermochemical state.

Numerical methodology

In the following sections, the versatility of the turbo-reactor will be demonstrated in its ability to operate effectively across a wide range of feedstocks and reaction conditions for various chemical processes powered by the RDR. The basic requirements for each process, based on the design of the datum stage, are summarised in Table 1. To evaluate the performance of the machine under these varying conditions without relying on computationally intensive reacting flow simulations, a framework has been developed to decouple the aerodynamics and chemical kinetics. This is introduced in the next section.

A decoupled framework for evaluating the effects of chemistry on aerothermal performance

A low-order approach is taken to decouple computational fluid dynamic (CFD) simulations and chemical kinetics. This is summarised in Figure 5 and can be explained as follows. Offline, 1-D detailed kinetic simulations are conducted for steam cracking (of an n-hexane and ethane feed), SMR, and ammonia decomposition

Table 1. Approximate preliminary requirements for the preheating and reaction zones based on the datum stage.

Feed/ process	Preheating zone (150°C < T < 900°C)			Reaction zone ($T \approx$ 900°C)		
	Approx. no. stages	Residence time (ms)	Enrgy-input (MJ kg^{-1})	Approx. no. stages	Residence time (ms)	Energy-input (MJ kg^{-1})
n-Hexane	8	4.0	2.4	6	11	1.8
Ethane	8	4.0	2.4	13	27	3.9
SMR: methane[a]	7	3.5	2.1	12–18	20–250	4.0–12.0
Ammonia[b]	8	4.0	2.4	12	170	3.6

[a]With Nickel catalyst[c]
[b]With Ruthenium catalyst[c].
[c]Surface-area-to-volume ratio = 400 m^{2}m^{-3}.

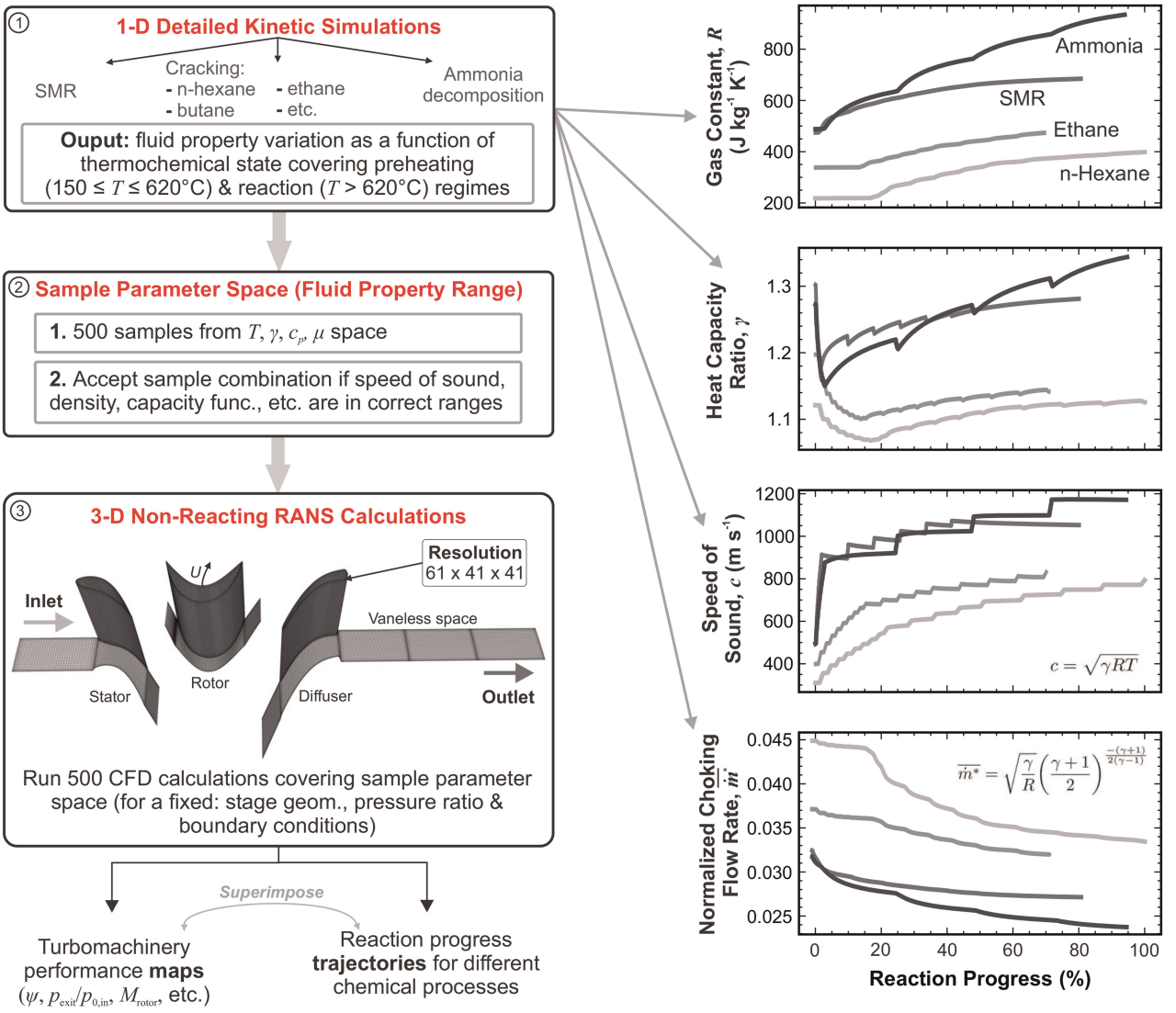

Figure 5. (Left) The methodology for constructing performance maps of the RDR for a broad range of chemical processes and reaction states and (Right) temperature-dependent variations in thermophysical properties, speed of sound, and non-dimensional choking mass flow rate w.r.t. reaction progress in the range 150–1,000°C.

reactions across a broad temperature range (150°C $\leq T \leq$ 1,000°C) covering both the preheating and reaction zones. All of the reactions are taken near completion to capture a broad range of reaction states.

The impact of the chemical reaction is effectively lumped into changes in the fluid properties, with four variables forming the parameter space: static temperature T, heat capacity ratio γ, isobaric specific heat capacity c_p and dynamic viscosity μ. By sampling from this fluid property space (see Figure 5) and performing a non-reacting CFD calculation for each sample, the performance can be evaluated under different reaction conditions without performing costly reacting flow simulations. The aerothermal performance of the turbomachine is characterised in the same way as conventional turbomachines using the non-dimensional groups shown in Equation 1 and defined in Dixon and Hall (2013):

Total pressure ratio

Reynolds number

$$\frac{p_{02}}{p_{01}}, \frac{\Delta T_0}{T_{01}}, \psi = f\left(\frac{\dot{m}\sqrt{\gamma R T_{01}}}{D^2 p_{01}}, \frac{\Omega D}{\sqrt{\gamma R T_{01}}}, Re, \gamma\right) \quad (1)$$

Stage loading coeff.

Capacity func.

Non-dim. blade speed

where p_0 is the total pressure, R is the gas constant, $\dot{m}$ is the mass flow rate, D is the mean diameter and Ω is the rotational speed. The terms highlighted in red are composition-dependent, indicating that turbomachinery performance is a direct function of the state of progress through each reaction. It is noted that there are two key implicit assumptions in this analysis. First, it is assumed that the aerodynamics and chemistry can be decoupled, and therefore are not assumed to be strongly interacting. Second, the fluid properties are assumed to be constant across a stage. In general, these are crude assumptions; however, these approximations allow us to gain rapid insight into how different reaction states change aerothermal performance.

Block (1): 1-D chemical kinetic modelling

For each feedstock and chemical process illustrated in Block (1) of Figure 5, a chemical reaction mechanism is automatically generated using RMG-PY (Gao et al., 2016). This includes both gas-phase reactions and heterogeneous surface-phase (catalytic) reactions. An in-house 1-D reactor model, built on top of a plug-flow reactor (PFR) model and a stiff ordinary differential equation solver within CANTERA (Goodwin et al., 2022), is used to approximate the enthalpy supplied by the rotor separated by user-defined time intervals representing the residence time per stage. Both ammonia decomposition and SMR require catalysts. For both, the surface-area-to-volume ratio is set to 400 m^2 m^{-3}, which could be tuned if required.

For each reaction, the validity of the semi-perfect gas assumption was analysed. The Redlich–Kwong real gas equation of state was used to simulate the gas mixtures at the relevant operating points. For almost all regimes, the compressibility factor Z and fugacity coefficient Φ deviated by less than 2% from their ideal gas values. For SMR, at low temperatures of $T \leq$ 200°C and at high pressures of 30 bar, the deviation from ideality increased to a maximum of ≈8% for Z and Φ. However, the error quickly dropped to a negligible level once the temperature rose by 100°C. This provides confidence in the semi-perfect gas assumption over an extensive range of conditions and feedstocks.

Block (2): sampling the fluid property space

The parameter space is formed by randomly sampling T, γ, c_p, and μ. As the non-dimensional groups on the right-hand side of Equation 1 involve *combinations* of these parameters, such as the stagnation speed of sound $\sqrt{\gamma R T_{01}}$, only samples where the capacity function, speed of sound, non-dimensional blade speed, etc., fall within the known ranges, are accepted. These *known ranges* are determined from precursor 1-D chemical kinetic simulations covering a range of feedstocks and feed conversion states (see previous section).

Block (3): 3-D steady non-reacting RANS CFD modelling

To evaluate aerothermal performance, 500× steady three-dimensional, non-reacting RANS calculations using a single stage were performed for each sample in the parameter space (see Block (3) in Figure 5). This was achieved

using the flow solver TBLOCK (Denton, 1983, 1986, 1992) with a mixing-length turbulence treatment. The mixing length-scale is tuned on a block-basis and is set by the turbulent length scale calculated from high-fidelity LES. The computational setup, which employed a simplified computational domain and numerical treatment, allowed hundreds of CFD simulations to be run within a few hours. To assess mesh independence, three grades of mesh density were simulated. The mass-averaged flow coefficient, stage loading coefficient, and rotor exit Mach number error were within 0.7%, 1.9%, and 2.0%, respectively. This gives us confidence in the trends presented in the following sections.

Although the mesh is relatively coarse and the turbulence modelling relatively simple, it is emphasised that the main objective is to determine qualitative trends rather than absolute values. Moreover, the main quantity of interest is the bulk work coefficient, which is found to be less sensitive to turbulence modelling and mesh density for the impulse-type blades used here.

Robustness of the turbo-reactor concept to feed variability

This paper presents the first instance in turbomachinery in which the flow is reacting across the majority of the gas path length. This results in significant variations in the thermophysical fluid properties from inlet to outlet. These changes cover a broad range of molecular weights; therefore, leading to reaction-dependent variations on turbomachinery performance, more specifically, due to changes in the gas dynamics ($c = \sqrt{\gamma RT}$, γ, $\overline{\dot{m}^*}$, etc.). In this section, we demonstrate the controllability of the machine over a broad range of Reynolds numbers, Mach numbers, and flow coefficients to illustrate the robustness of the concept to feed variability.

Influence of Reynolds number on aerodynamic performance

The Reynolds number $Re = \rho V b/\mu$ (based on the stator exit conditions and true blade chord) varies with feed composition and reaction progress due to changes in fluid density and dynamic viscosity. Figure 6a suggests that stage loading is weakly dependent on Reynolds number over a wide range ($1 \times 10^4 \leq Re \leq 2.5 \times 10^6$), dropping by only 9% over the investigated range. As expected, more energy can be imparted into the fluid at high Reynolds numbers. Figure 6b indicates that this is because, in the low Reynolds number regime, there is a higher level of flow separation as the boundary layer is more sensitive and cannot negotiate local adverse pressure gradients. Higher flow separation leads to higher blockage and lower throughflow capacity, as well as increased flow deviation. Since stage loading scales with flow coefficient and flow turning, the specific energy input falls at low Reynolds numbers. However, the change is relatively minor (see Figure 6a).

Aerothermal performance maps covering a wide operating range

This section demonstrates the applicability of using a turbomachine for four different chemical processes using a uniform stage design, fixed annulus flow area, and fixed boundary conditions. These conditions include a fixed imposed pressure ratio $p_{exit}/p_{0,in} \approx 0.98$ and blade tip speed. As highlighted at the bottom right of Figure 7, by varying the fluid properties (see Figure 5) while fixing $p_{exit}/p_{0,in}$, the system naturally experiences variations in the operating point, set by the flow coefficient $\phi = V_x/U$. This variation is exploited to probe the response of the dynamical system (i.e., the RDR) subject to input perturbations (i.e., fluid properties). As a result, the

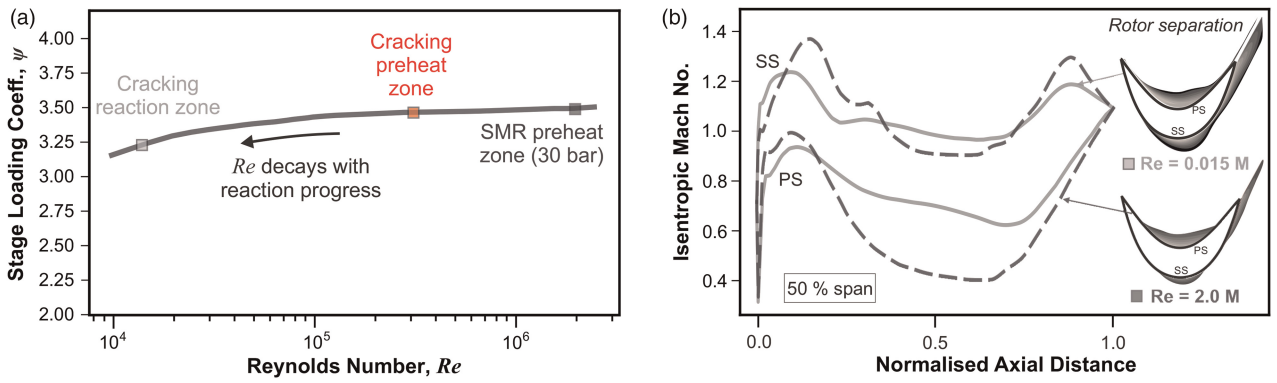

Figure 6. (a) Variation of stage loading coefficient with Reynolds number and (b) the isentropic Mach number distribution for two extreme Reynolds number states, corresponding to different reactions powered by the RDR.

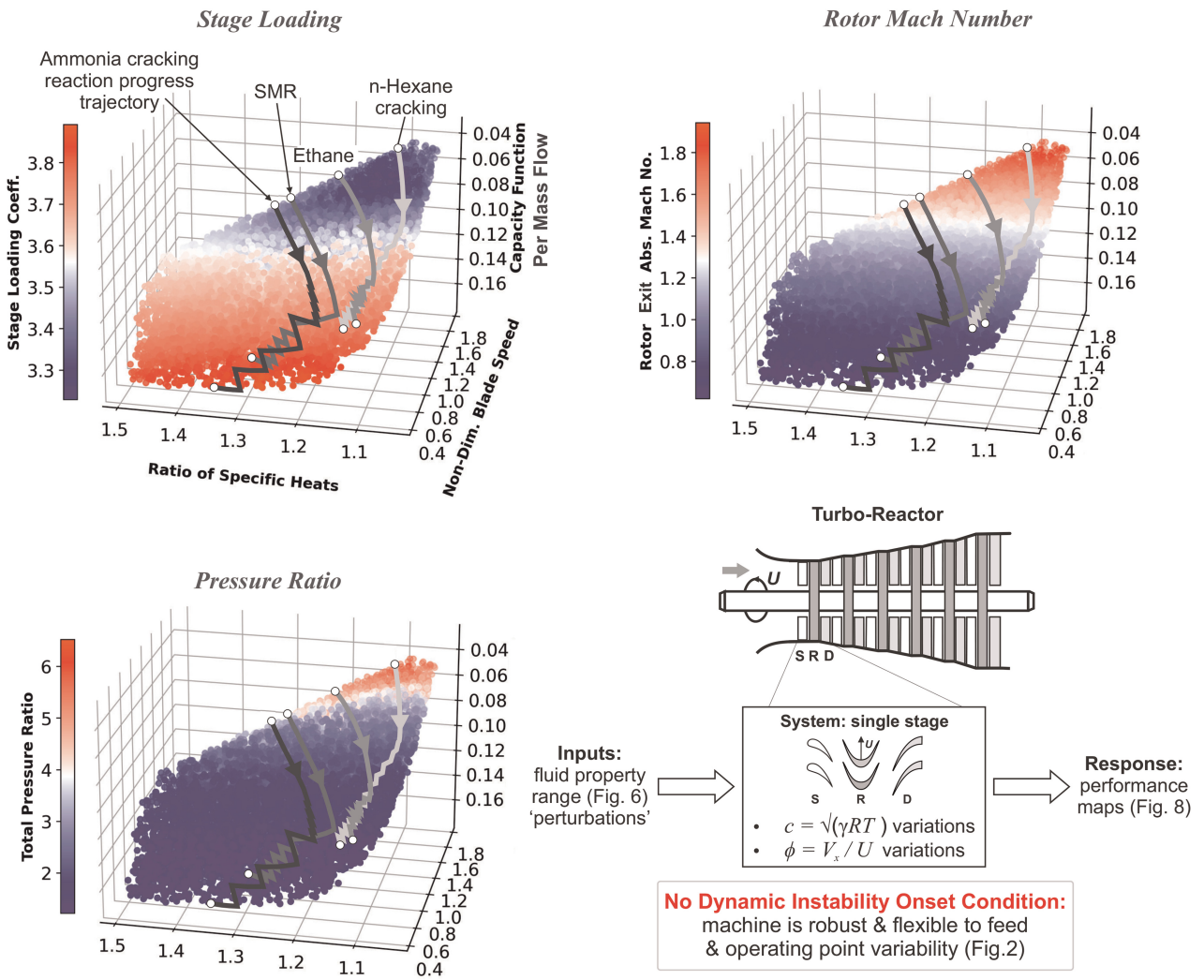

Figure 7. Aerothermal performance maps showcasing the reaction-progress trajectories with thick solid lines for four applications of the turbo-reactor (for a fixed *Re* = 100,000 and pressure ratio $p_{\text{exit}}/p_{0,\text{in}} = 0.98$).

robustness and controllability of the machine can be demonstrated over a wide range of fluid properties and hence operating regimes. Of course, during normal operation, the delivery pressure, stage design, and annulus flow area can be customised for each stage and for each chemical reaction to maintain and match the optimum velocity triangles.

Each thick solid line indicated in Figure 7 represents the trajectory through non-dimensional parameter space using decoupled detailed 1-D kinetic calculations. This detailed chemical analysis is performed independently, and the results are superimposed on the performance maps. These lines effectively illustrate how aerothermal performance varies along the streamwise direction across a multistage machine for each chemical process. For all reactions, the imposed pressure ratio is fixed; therefore, the Mach number decays across the multistage machine. Since density decreases and the flow area is fixed, this is accompanied by an increase in the flow coefficient toward the rear of the machine. Therefore, the stage loading is higher near reaction completion. At the beginning of the reaction, the feeds are initially separated in the non-dimensional parameter space (see Figure 7). However, as the reactions progress, they all converge toward the higher loading region.

More generally, two insights can be gained from the response of the performance metrics shown in Figure 7. First, the ratio of specific heats has a relatively small impact on the stage loading. Secondly, the dominant parameters driving changes in flow physics are the non-dimensional blade speed and flow coefficient. The non-dimensional blade speed is inversely proportional to the speed of sound (see Figure 5 and Equation 1) and varies by almost a factor of 4.5, whilst the flow coefficient, which sets the velocity triangles, varies by almost a factor of 2 (due to the density variation). The stage loading coefficient does not respond significantly, with a maximum deviation of 15%, illustrating the robustness of the turbo-reactor despite the use of a fixed elemental stage. This margin can be further reduced by adjusting the delivery pressure and modifying the flow area to match the flow

coefficient and the restore the velocity triangles. Since there is no onset condition for violent system instability (see Figure 4c), the machine can provide a high enthalpy input over a broad range of reaction and operating states.

Parameter space boundaries: extremes of the Mach number regime

Two extreme Mach number regimes, covering a wide range of feed molecular weights (2.0–86.0 g mol^{-1}) and hence the speeds of sound (280–1,150 ms^{-1}), are selected from the parameter space shown in Figure 7 and are compared in more detail in Figure 8. The low Mach number regime corresponds to an ammonia feed toward reaction completion, and the high Mach number regime corresponds to an n-hexane feed before the reaction starts. The first case represents a front stage of the machine, which is capacity-limiting due to the low speed of sound (see Figure 5 (*Right*)), and the second case represents a rear stage. The high Mach number case (see Figure 8 (*Right*)) is presented to illustrate the robustness of the flow at off-design regimes. However, in practice, the mismatched velocity triangles can be partially corrected by adjusting the delivery pressure to accommodate a higher mass flow rate, increasing the annulus flow area, and/or increasing the throat area to raise the swallowing capacity near the choke point.

Figure 8 provides three key insights into the flow physics of the system. First, within the rotor, the low Mach number case is mainly affected by PS separation and blockage, whereas for the high Mach number case, an increased positive incidence angle results in a higher level of SS separation contaminating the flowfield. This is because (I) the flow coefficient drops by almost a factor of 2 for the high Mach number case (II) the Mach number is supersonic, making the flow sensitive to small changes in incidence ($\leq$1.5°), and (III) a shockwave at the rotor inlet contributes to further SS boundary layer separation through shockwave boundary layer interaction (SWBLI).

Second, the gas mixture in the low Mach number regime (Figure 8 (*Left*)) consists of 70% hydrogen on a mole basis. As hydrogen has a low molecular weight and hence a high speed of sound, it can accommodate a higher flow coefficient at a given pressure ratio and a fixed annulus area. This allows for a greater change in tangential velocity whilst avoiding the SWBLI in the rotor, resulting in higher stage loading (see Figure 8). As the flow is far below the choking limit, an even higher flow coefficient can be achieved by increasing the delivery pressure (see Figure 4b). Therefore, it is evident that the local fluid properties (set by the local composition state)

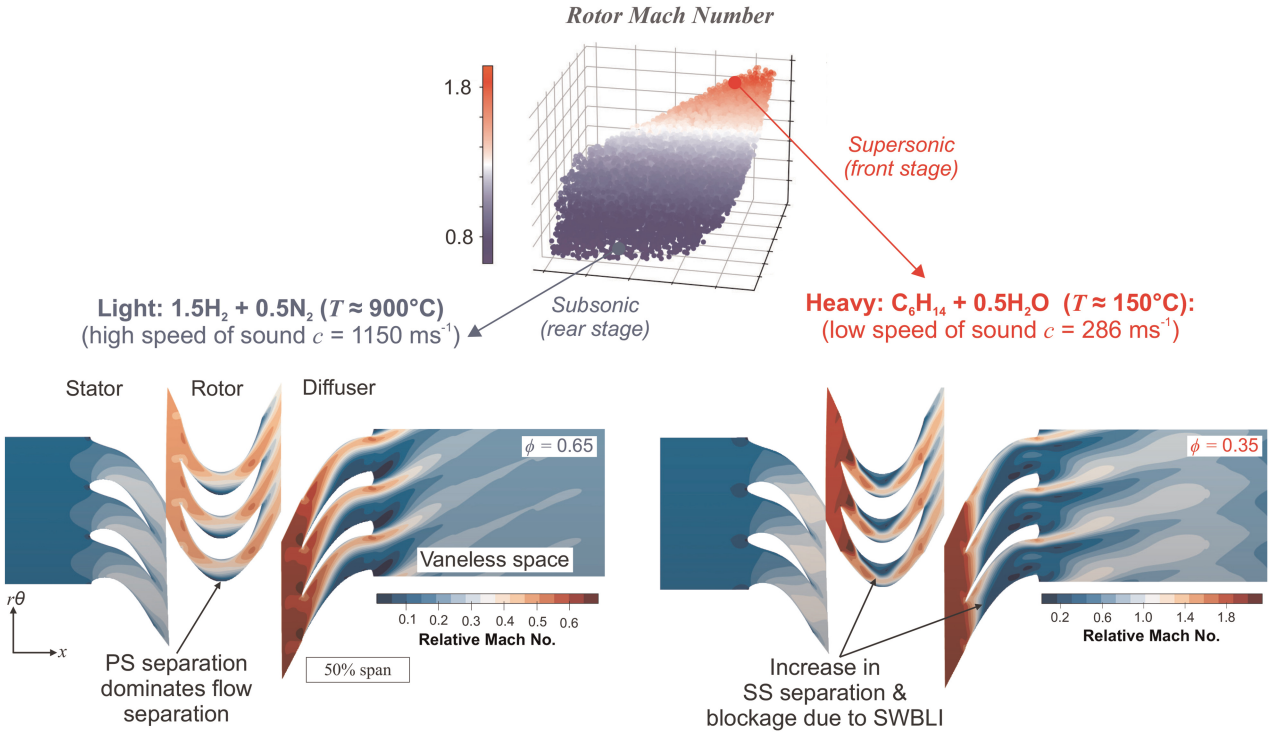

Figure 8. Comparison of the midspan relative Mach number distribution at two "extreme" corners of the parameter space where the fluid properties and local gas composition lead to two polar speed of sound regimes.

have a significant influence on the operating range, compressibility, and loading capability for a fixed geometry. With the current datum design, the operating range of the high molecular weight n-hexane feed (Figure 8 (*Right*)) is more restricted, and the $\phi - \psi$ characteristic is almost vertical (see the low speed of sound boundary in Figures 4b and 4c). However, for a given fluid, the design can be altered to balance the operating range and the specific energy input rate per stage.

Finally, the results presented demonstrate that the RDR can still achieve a reasonably high level of specific energy input ($\Delta h_0 \approx 220$ kJ kg^{-1}) despite large-scale flow separation due to incidence and SWBLI, as indicated in Figure 8 (*Right*). This flexibility of the machine is a direct consequence of the fact that isentropic efficiency does not impact the performance of the machine. Without a requirement to resist an adverse pressure gradient, entropy can be generated without dramatic repercussions for the specific energy that can be imparted into the fluid. Despite an elevated level of flow separation within the passage, the flow within the rotor is turned through an angle close to the blade metal angles. Therefore, the specific energy imparted into the fluid remains high, albeit at the expense of a reduced flow coefficient due to blockage. In the high Mach number regime, a higher total pressure ratio across the rotor (see Figure 7) results in an increased local choking mass flow rate. This ensures that a reasonable level of mass can still be swallowed, despite a reduction in the effective throat area due to blockage in the diffuser. As the total pressure is rapidly dissipated downstream, there is no global adverse pressure gradient, as discussed in the next section.

A breakdown of the energy conversion mechanisms

Once the kinetic energy (KE) has been absorbed by the flow through the rotor, it must eventually dissipate into internal energy u within the diffuser and vaneless space. In some configurations of the machine, such as the ultra-fast gas preheating zone before the reaction starts, the vaneless space can be removed, and the majority of the energy dissipation occurs every 2–4 stages. In contrast, for a gas mixture undergoing reactions, it is more optimal to dissipate the mechanical energy at every stage to repeatedly balance and compensate for the drop in temperature caused by the reaction.

A well-designed energy transformation system aims to convert kinetic energy into internal energy over the minimum possible time scale, typically less than 0.5 ms. This is achieved controllably through both an isentropic pressure rise and through entropic dissipation mechanisms equivalent to aerodynamic losses. By increasing the entropic rise ds, the increase in static temperature dT can be maximised within a minimum time scale while removing any minor unwanted gains in static pressure dp. This principle can be expressed by the Gibbs equation $c_p dT = (1/\rho)dp + Tds$. Exploiting aerodynamic losses in this way is in stark contrast to conventional energy-imparting machines.

Figure 9 illustrates an approximate breakdown of the energy conversion mechanisms at the two flow regimes shown earlier in Figure 8 above. The energy conversion breakdown is determined by integrating the viscous dissipation rate $\dot{S}_{\mathrm{vsic}}$ (Denton, 1993) zonally for five regions in the diffuser-vaneless-space system listed in Figure 9 (*Left*). A more detailed description of the "loss audit" methodology can be found in Moore and Moore (1983) and Pullan et al. (2004). The sixth energy conversion mechanism accounted for is the isentropic pressure rise $\zeta_{\mathrm{isentropic}}$ (see Equation 2), which is calculated using isentropic relations between two known states. Other conversion sources, such as tip leakage, are neglected.

$$\zeta_{\mathrm{isentropic}} = \frac{c_v \Delta u_{\mathrm{isentropic}}}{h_{0,\mathrm{rotor}} - h_{\mathrm{rotor}}} \tag{2}$$

Equation 3 is used to calculate the entropic portion $\zeta_{\mathrm{entropic}}$ of the total energy conversion coefficient $\zeta = \zeta_{\mathrm{isentropic}} + \zeta_{\mathrm{entropic}}$. It is noted that the subscript $(_{\mathrm{rotor}})$ refers to the rotor exit station.

$$\zeta_{\mathrm{entropic}} = \frac{\dot{S}_{\mathrm{vsic}}}{\dot{m}(h_{0,\mathrm{rotor}} - h_{\mathrm{rotor}})}, \quad \text{where} \quad \dot{S}_{\mathrm{visc}} = \iiint_v \tau_{ij} \frac{dV_i}{dx_j} dv \tag{3}$$

Figure 9 illustrates the differences in the energy conversion mechanisms for two feeds at different reaction states. In the subsonic case (i.e., high-temperature decomposed ammonia), isentropic energy conversion dominates since the flow in the blade passage is more attached. For the supersonic case, there is still a contribution from isentropic pressure rise, but the contribution is smaller, and the mechanism is dominated by pressure rise due to the isentropic component of the shockwave action rather than diffusion induced by changes in the effective flow area.

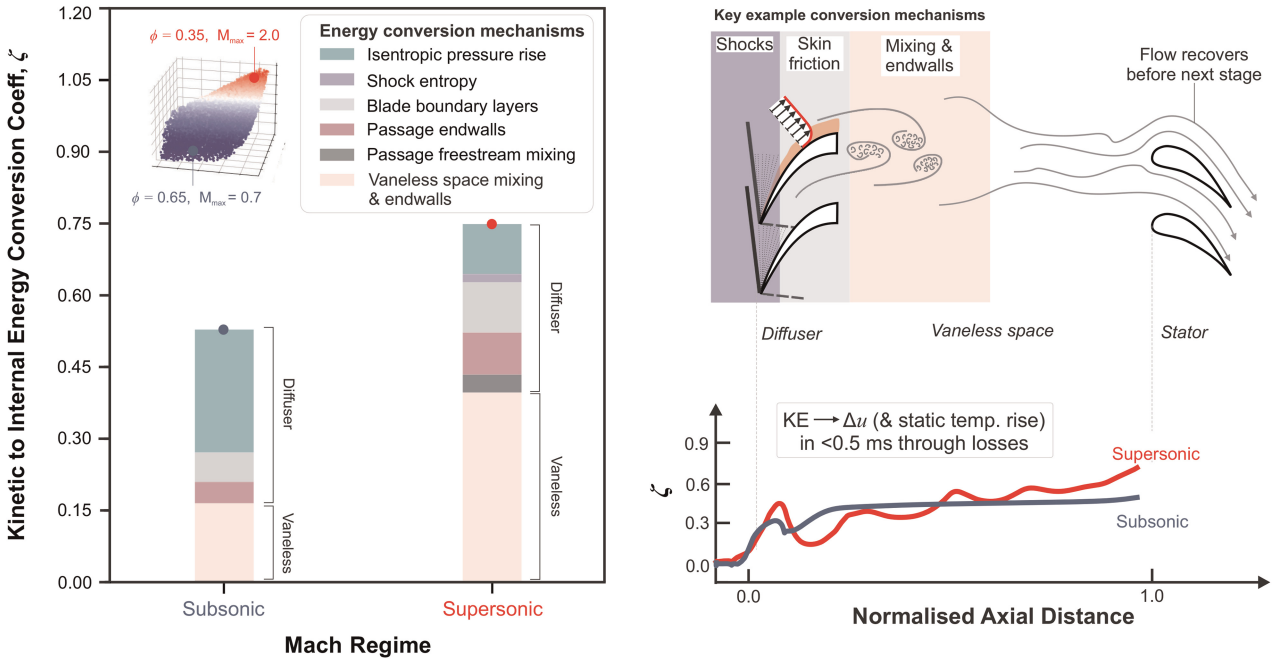

Figure 9. A breakdown of kinetic energy (KE) to internal energy ($\Delta u = c_v \Delta T$) conversion mechanisms including both entropic dissipation and isentropic pressure rise contributions. The breakdown for a single stage is compared for two extreme Mach regimes corresponding to thermophysical properties encountered for two different reactions.

In both cases, the energy conversion due to trailing edge (TE) mixing is large since the TE is thick (42% of the blade pitch), blunt and square. In the supersonic case, this energy conversion source is well over 50% of the total energy conversion. This is significantly higher than the subsonic case as TE mixing loss scales with Mach number Denton and Xu (1990). In the supersonic case, the entropy generated through the shock is relatively small, meaning that the *direct* impact of the shock is minor. However, there is a substantial *indirect* impact from the shockwave due to shock-induced boundary layer separation. This significantly enhances boundary layer dissipation as well as downstream mixing.

This analysis shows that, despite variations in the incoming dynamic head over a wide range of operating points and feeds, almost 60% of the rotor exit kinetic energy can be dissipated into internal energy over a short distance (<50 mm). In different regimes, the flow self-adjusts the contributions from each conversion mechanism to match the downstream boundary condition. Future work will investigate the energy conversion mechanisms in more detail.

Summary and conclusions

This study has demonstrated the feasibility of using an electric-motor-driven turbomachine to mitigate carbon emissions and improve the operability, controllability, and reaction performance of four crucial energy-intensive endothermic reaction processes. The numerical investigation presented in this paper has revealed several key design characteristics of the concept summarised in Figure 10, which are as follows:

1. It has been shown that a universal stage design philosophy can be used for a wide range of feeds and reaction states. The specific energy input remains relatively high over a wide range of conditions. Since the collection of molecular weights covered is extensive, many other relevant chemical and non-chemical processes should fall within this range.
2. The robustness of the turbomachine has been successfully demonstrated over a wide range of operating and Mach number regimes by inducing operating point excursions through fluid property perturbations. The stage loading only dropped by 15% over a broad set of flow conditions, indicating the flexibility of the RDR. Additionally, the turbomachine showed a weak dependence on the Reynolds number, with only a 9% variation in the work coefficient over two orders of magnitude of the Reynolds number.
3. Without a requirement for pressure gain, the design restrictions of efficiency and system instability are no longer relevant. Therefore, a high level of incidence and separation can be endured, facilitating a high level of

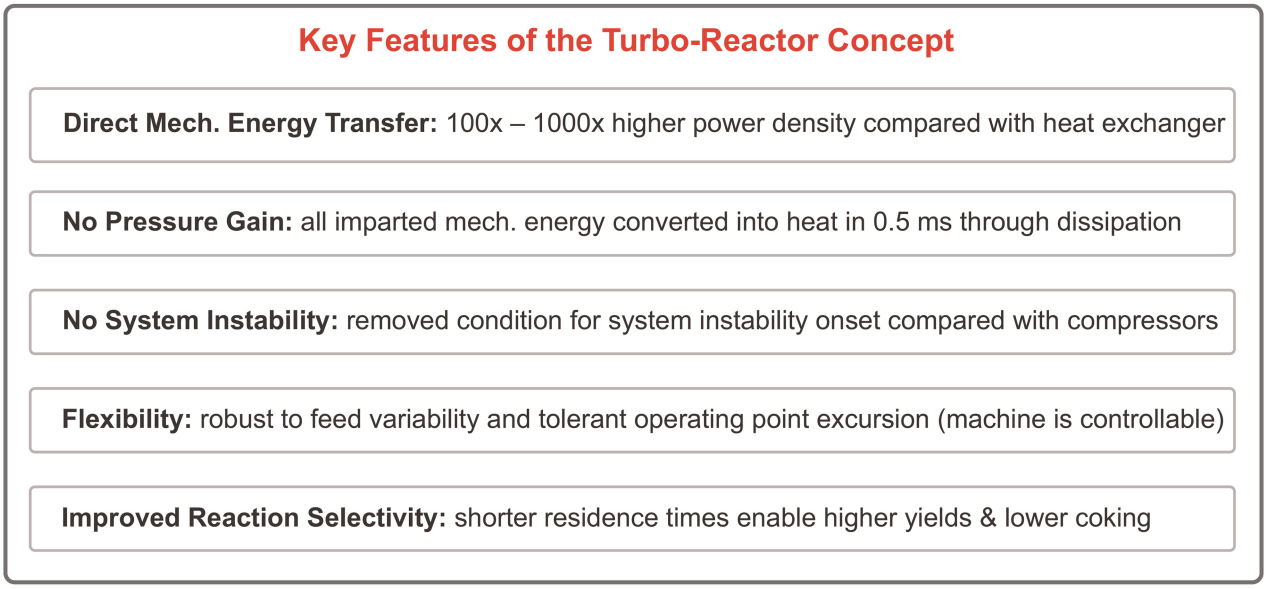

Figure 10. Schematic block diagram summarising the key features of the new RDR concept.

energy input and swallowing capacity over the operating range. The limits of the RDR are set only by choking (which is a restriction on the throughflow capacity of the machine) and not by system instability. Of course, local flow instability within certain blade rows may still occur.

4. Over a broad range of gas velocities and Mach numbers—corresponding to different feeds and reaction states—this work has shown that kinetic energy can be dissipated into internal energy (and static temperature rise) over an extremely short time scale of 0.5 ms, enabling a compact machine for ultra-fast gas heating. The processing mechanisms self-adjust in different flow regimes.

In summary, a turbomachine is a robust and efficient means of heating a wide variety of (endothermically) *reacting* gas mixtures to high temperatures. This analysis covers a broad spectrum of fluid properties, therefore suggesting that a similar elemental stage design could also be used to heat other *non-reacting* gas mixtures, enabling decarbonisation of energy-intensive industries, such as steel, cement, glass, and aluminium, while simultaneously reducing the volume 50 to 1,000 times relative to conventional surface heat exchangers.

Nomenclature

Symbols

b	true blade chord, m
$c = \sqrt{\gamma RT}$	speed of sound, m s^{-1}
$C_{\psi_{TS}} = \frac{p_{exit} - p_{0,in}}{0.5\rho U^2}$	total-to-static pressure rise coefficient
c_p	isobaric heat capacity, J kg^{-1} K^{-1}
c_v	isochoric heat capacity, J kg^{-1} K^{-1}
h_0	stagnation enthalpy, J kg^{-1}
$\underline{\Delta_{rxn}H^0_{298}}$	enthalpy of reaction, J kg^{-1}
$\dot{m}^*$	non-dimensional choking mass flow rate
p	static pressure, Pa
p_0	stagnation pressure, Pa
R	specific gas constant, J kg^{-1} K^{-1}
$Re = \frac{\rho V b}{\mu}$	Reynolds number
$\dot{S}_{vsic}$	viscous dissipation rate, W
T	static temperature, K
Δu	internal energy change, J kg^{-1}
U	mean blade speed, m s^{-1}
v	domain volume, m^3
V	absolute velocity, ms^{-1}

V_x	axial velocity, ms^{-1}
$\gamma = \frac{c_p}{c_v}$	heat capacity ratio
ζ	energy conversion coefficient
μ	dynamic viscosity, Pa s
$\psi = \frac{\Delta h_0}{U^2}$	stage loading/work coefficient
$\phi = \frac{V_x}{U}$	flow coefficient
τ_{ij}	shear stress tensor, Pa

Acronyms

PFR	plug-flow reactor
PS/SS	pressure/suction surface
RDR	RotoDynamic Reactor (turbo-reactor)
SMR	steam methane reforming
SWBLI	shockwave boundary layer interaction

Acknowledgments

The authors thank Coolbrook Oy for supporting this work. The authors are grateful for fruitful discussions with Tuomas Ouni at Coolbrook Oy.

Funding sources

Coolbrook Oy.

Competing interests

Dylan Rubini declares that he has no conflicts of interest. Nikolas Karefyllidis declares that he has no conflicts of interest. Budimir Rosic declares that he has no conflicts of interest. Liping Xu declares that he has no conflicts of interest. Elina Nauha declares that he has no conflicts of interest.

References

Bender M. (2014). An overview of industrial processes for the production of olefins–C4 hydrocarbons. *ChemBioEng Reviews*. 1 (4): 136–147. https://doi.org/10.1002/cben.201400016.

Bushuev V. A. (2016). Bladed Reactor for the Pyrolysis of Hydrocarbons. U.S. Patent Application No. US 9.494,038 B2. Washington, DC: U.S. Patent and Trademark Office.

Coolbrook Oy. (2022). Coolbrook Oy. Helsinki, Finland, accessed Oct. 15, 2022, https://coolbrook.com.

Delikonstantis E., Scapinello M., and Stefanidis G. D. (2019). Process modeling and evaluation of plasma-assisted ethylene production from methane. *Processes*. 7 (2): 68. https://doi.org/10.3390/pr7020068.

Denton J. D. (1983). An improved time-marching method for turbomachinery flow calculation. *ASME Journal of Engineering for Power*. 105 (3): 514–521. https://doi.org/10.1115/1.3227444.

Denton J. D. (1986). The use of a distributed body force to simulate viscous effects in 3D flow calculations. In Vol. 1 Turbomachinery of Turbo Expo: Power for Land, Sea, and Air. p. V001T01A058. https://doi.org/10.1115/86-GT-144.

Denton J. D. (1992). The calculation of three-dimensional viscous flow through multistage turbomachines. *ASME Journal of Turbomachinery*. 114 (1): 18–26. https://doi.org/10.1115/1.2927983.

Denton J. D. (1993). The 1993 IGTI scholar lecture: loss mechanisms in turbomachines. *Journal of Turbomachinery*. 115 (4): 621–656. https://doi.org/10.1115/1.2929299.

Denton J. D., and Xu L. (1990). The trailing edge loss of transonic turbine blades. *Journal of Turbomachinery*. 112 (2): 277–285. https://doi.org/10.1115/1.2927648.

Dixon S. L., and Hall C. (2013). Fluid Mechanics and Thermodynamics of Turbomachinery. Butterworth-Heinemann: Oxford.

Gao C. W., Allen J. W., Green W. H., and West R. H. (2016). Reaction mechanism generator: automatic construction of chemical kinetic mechanisms. *Computer Physics Communications*. 203: 212–225. https://doi.org/10.1016/j.cpc.2016.02.013.

Goodwin D. G., Moffat H. K., Schoegl I., Speth R. L., and Weber B. W. (2022). Cantera: An object-oriented software toolkit for chemical kinetics, thermodynamics, and transport processes. https://www.cantera.org. Version 2.6.0.

Greitzer E. M., Tan C. S., and Graf M. B. (2007). Internal flow: concepts and applications.

IEA (2021). Global Energy Review 2021, Technical Report. International Energy Agency (IEA), Paris.

IEA (2022). Hydrogen, Paris, Technical Report. International Energy Agency (IEA), Paris.

Jackson C., Fothergill K., Gray P., Haroon F., Makhloufi C., et al. (2019). Ammonia to Green Hydrogen Project: Feasibility Study. UK: Ecuity.

Karefyllidis N., Rubini D., Rosic B., Xu L., and Purola V.-M. (2023). A novel axial energy-imparting turbomachine for high-enthalpy gas heating: robustness of the aerodynamic design. *Journal of Turbomachinery*. 146(3): 031005. https://doi.org/10.1115/1.4063928.

Kusenberg M., Zayoud A., Roosen M., Thi H. D., Abbas-Abadi M. S., et al. (2022). A comprehensive experimental investigation of plastic waste pyrolysis oil quality and its dependence on the plastic waste composition. *Fuel Processing Technology*. 227: 107090. https://doi.org/10.1016/j.fuproc.2021.107090.

Lu Q., Zhang B., Yang S., and Peng Z. (2022). Life cycle assessment on energy efficiency of hydrogen fuel cell vehicle in china. *Energy*. 257: 124731. https://doi.org/10.1016/j.energy.2022.124731.

Moore J. and Moore J. G. (1983). Entropy production rates from viscous flow calculations: part I — a turbulent boundary layer flow. In Vol. 1 Turbomachinery of Turbo Expo: Power for Land, Sea, and Air. V001T01A032. https://doi.org/10.1115/83-GT-70.

Pullan G., Denton J., and Curtis E. (2004). Improving the performance of a turbine with low aspect ratio stators by Aft-loading. *Journal of Turbomachinery*. 128 (3): 492–499. https://doi.org/10.1115/1.2182000.

Rostrup-Nielsen J., and Christiansen L. J. (2011). Vol. 10. *Concepts in Syngas manufacture*. London: World Scientific.

Rubini D., Karefyllidis N., Xu L., Rosic B., and Johannesdahl H. (2022a). Accelerating the development of a new turbomachinery concept in an environment with limited resources and experimental data: challenges. In Vol. 86120. Turbo Expo: Power for Land, Sea, and Air. American Society of Mechanical Engineers. V10DT36A001.

Rubini D., Karefyllidis N., Xu L., Rosic B., and Johannesdahl H. (2022b). A new robust regenerative turbo-reactor concept for clean hydrocarbon cracking. *Journal of the Global Power and Propulsion Society*. 6: 135–150. https://doi.org/10.33737/jgpps/150550.

Rubini D., Xu L., Rosic B., and Johannesdahl H. (2021). A new turbomachine for clean and sustainable hydrocarbon cracking. *ASME Journal of Engineering for Gas Turbines and Power*. 144 (2): 021024. https://doi.org/10.1115/1.4052784.

Thiel G. P. and Stark A. K. (2021). To decarbonize industry, we must decarbonize heat. *Joule*. 5 (3): 531–550. https://doi.org/10.1016/j.joule.2020.12.007.

Venkataraman K., Wanat E., and Schmidt L. (2003). Steam reforming of methane and water-gas shift in catalytic wall reactors. *AIChE Journal*. 49 (5): 1277–1284. https://doi.org/10.1002/aic.690490518.

Weydahl T., Jamaluddin J., Seljeskog M., and Anantharaman R. (2013). Pursuing the pre-combustion ccs route in oil refineries–the impact on fired heaters. *Applied Energy*. 102: 833–839. https://doi.org/10.1016/j.apenergy.2012.08.044.